Available online at www.sciencedirect.com
ScienceDirect
Mathematics and Computers in Simulation 81 (2011) 2051–2061
MATHEMATICS AND COMPUTERS IN SIMULATION
www.elsevier.com/locate/matcom

An Unfitted Discontinuous Galerkin method for pore-scale simulations of solute transport

Peter Bastian, Christian Engwer*, Jorrit Fahlke, Olaf Ippisch

Interdisciplinary Center for Scientific Computing, University of Heidelberg, Im Neuenheimer Feld 368, D-69120 Heidelberg, Germany

Received 8 December 2009; received in revised form 29 June 2010; accepted 8 December 2010
Available online 31 December 2010

Abstract

For the simulation of transport processes in porous media effective parameters for the physical processes on the target scale are required. Numerical upscaling, as well as multiscale approaches can help where experiments are not possible, or hard to conduct.

In 2009, Bastian and Engwer proposed an Unfitted Discontinuous Galerkin (UDG) method for solving PDEs in complex domains, e.g. on the pore scale. We apply this method to a parabolic test problem. Convergence studies show the expected second order convergence. As an application example solute transport in a porous medium at the pore scale is simulated.

Macroscopic breakthrough curves are computed using direct simulations. The method allows finite element meshes which are significantly coarser then those required by standard conforming finite element approaches. Thus it is possible to obtain reliable numerical results for macroscopic parameter already for a relatively coarse grid.

Keywords: Discontinuous Galerkin method; Higher order; Unfitted finite elements; Numerical upscaling; Flows in porous media; Convection–diffusion-problems; Parabolic equations

1. Introduction

1.1. Motivation

The correct prediction of solute transport in porous media is important for many different applications like groundwater contamination and remediation. On the continuum scale solute transport is commonly simulated using the convection–dispersion equation. Two major difficulties arise in this approach: (i) It is hard to determine the correct dispersion coefficient, which depends not only on the solute itself but also on the porous medium and the flow velocity. (ii) The convection–dispersion equation is only valid in the limit of travel distances which are large enough for the solute to sample all the heterogeneities of the porous medium. On shorter travel distances one often experiences anomalous dispersion with an earlier breakthrough and a long tailing [16,26].

Pore scale modeling of water and solute transport is a helpful tool to derive macroscopic parameters like the dispersion coefficient as well as to study the anomalous dispersion. At the pore scale water transport is described by the (Navier) Stokes equation, solute transport by the convection–diffusion equation. While a plausible microscopic structure was

* Corresponding author.
E-mail address: christian.engwer@iwr.uni-heidelberg.de (C. Engwer).

0378-4754/$36.00
doi:10.1016/j.matcom.2010.12.024

formerly often generated artificially it can be obtained nowadays with a sufficient resolution by high-resolution X-ray tomography [25,19].

1.2. Pore scale simulations

In the last years different approaches have been developed to simulate water and solute transport at the pore scale. Pore network models represent the pore space as a network of usually cylindrical pores (pore throats) which connect spherical pore bodies. The network is generated to resemble the pore size distribution of the real porous medium and therefore is only similar to the original porous medium. Transport in the pores is calculated from simplified flow models like Hagen–Poiseuille. While the vast majority of pore network model applications is targeted at water transport, they have also been used to simulate solute transport, see e.g. [8,24,1].

Lattice-Boltzmann methods (LBM) simulate water and solute transport as the movement and collision of a number of discrete fictitious particles along a highly interconnected lattice. The collision operator is chosen to obtain a solution of the partial differential equations. LBM were applied to a range of applications, like computation of dispersion tensors [9,13,26], or reactive transport [14,15].

Another particle based but mesh-free method is smoothed-particle hydrodynamics, where the fluid is divided into a set of discrete particles. The movement of each particle is simulated in a Lagrangian approach [27,23]. The method is popular in computer graphics but requires a high number of particles to produce accurate results.

For fluid flow in porous media also simulation codes exist which implement Finite-Difference, Finite-Volume and Finite-Element discretizations [22]. However, the generation of suitable grids for complex pore spaces can be quite demanding and can result in a very high number of unknowns.

Manwart et al. [17] compared a Finite-Difference and a Lattice-Boltzmann model for the simulation of pore scale transport to determine the effective permeability of porous media. They found that the computation time is similar for both the Finite-Differences and the LBM, which needs more memory. A comparison of a Finite-Volume, Finite-Element and Lattice Boltzmann code by Geller et al. [12] showed that LBM can be rather inefficient for simulations of laminar steady-state flow fields.

Handling the pore space domain in a numerical simulation is not easy. On the pore scale the solid phase forms a complex shaped geometry. Within pore scale simulations a good approximation of the geometrical shape is crucial to obtain reliable numerical results. Sharp edges in the geometry lead to singularities in the solution, which disturb the whole solution due to the internal friction of the fluid. Obtaining a good approximation of the resulting domain usually requires simulations on a very fine grid, while the interest on the other hand lies only in macroscopic parameters, which could be calculated with a sufficient precision from a solution on a much coarser mesh.

In [6], Bastian and Engwer proposed an Unfitted Discontinuous Galerkin (UDG) method for PDEs on domains with a complicated geometric shape. It combines the Unfitted Finite Elements Method [3] with a Discontinuous Galerkin (DG) discretization and allows to construct the finite element mesh independently of the geometry. In [6], the UDG method was presented for elliptic problems. An application to pore scale simulations, i.e. numerical upscaling for the stationary Stokes equation, is published in [11].

In this paper the UDG approach is applied to a time dependent problem on complicated geometries, as they can be found in pore scale simulations. It is implemented on top of the DUNE software framework [5,4] and is available as a separate DUNE Module. In the following section we state our parabolic model problem. Then the space and time discretization, and especially the employed UDG scheme, will be described. In Section 4 convergence studies and application on a simplified pore space geometry are presented.

2. Model problem

We consider the convection–diffusion equation as a model problem for parabolic partial differential equations. We will refer to it as the "transport equation"

$$\partial_t c + \nabla \cdot \mathbf{j} = 0 \qquad \text{in } \Omega \tag{1a}$$

$$\mathbf{j} = \mathbf{u}c - D\nabla c, \qquad \text{in } \Omega \tag{1b}$$

and we consider Dirichlet, Neumann and outflow boundary conditions

$$\mathbf{j}\cdot\mathbf{n} = (\mathbf{u}c - D\nabla c)\cdot\mathbf{n} \qquad \text{on} \quad \Gamma_O = \partial\Omega \text{ where } \mathbf{u}\cdot\mathbf{n} > 0 \tag{1c}$$

$$c = c_0 \qquad \text{on} \quad \Gamma_D \subseteq \partial\Omega \setminus \Gamma_O \tag{1d}$$

$$\mathbf{j}\cdot\mathbf{n} = F \qquad \text{on} \quad \Gamma_N \subseteq \partial\Omega \setminus (\Gamma_O \cup \Gamma_D) \tag{1e}$$

where $\mathbf{u}$ denotes the velocity of the solvent, c is the concentration of the solute and $\mathbf{n}$ the outer normal to Ω. The transport of c is described by the flux $\mathbf{j}$, which consists of two parts. The first one is molecular diffusion, proportional to the gradient ∇c and parameterized by the diffusion coefficient D. The second part is convection which is proportional to a given velocity $\mathbf{u}$. We assume that the system is convection dominated.

Dirichlet boundary conditions specify a concentration c_0 on the boundary, for Neumann boundaries a flux F is prescribed. The special case $F = 0$ of the Neumann boundary condition is known as the "no-flux condition". The outflow boundary condition is applied where the velocity is pointing outwards. It is essentially a "do-nothing" boundary condition and allows the solute to leave the domain freely.

3. Numerical simulation

For the simulation of time dependent problems we use method of lines to handle time and space derivatives separately. For the time derivative one of the common implicit time stepping schemes is used. Space discretization is done using the Unfitted Discontinuous Galerkin method.

In the following subsection the Unfitted Discontinuous Galerkin Method (UDG) will be explained. Then we discuss the particular time and space discretizations chosen for the model problem.

3.1. The Unfitted Discontinuous Galerkin method

In 1987 [3] presented a conforming finite element method on an unfitted mesh, i.e. the finite element mesh did not resolve the geometry. Boundary conditions along the geometry were enforced weakly using Nitsche's method [18]. This method is known as the Unfitted Finite Element Method. However the method itself does only allow first order trial and test functions. The Unfitted Discontinuous Galerkin method [6] extends this idea by using Discontinuous Galerkin methods instead of Nitsche's method for the handling of essential boundary conditions. This does allow the use of higher order trial and test functions. For problems described by a conservation equation DG methods are especially attractive as many DG formulations are locally mass conservative and therefore able to accurately describe fluxes over element boundaries. For a thorough discussion of the DG method we refer to [2].

Given a domain $\Omega \subseteq \mathbb{R}^d$, $\mathcal{G}$ describes a disjoint partitioning into N sub-domains

$$\mathcal{G}(\Omega) = \left\{\Omega^{(0)}, \ldots, \Omega^{(N-1)}\right\}. \tag{2}$$

The partitioning $\mathcal{G}$ is usually based on geometrical properties obtained from experiments or previous simulations. The boundaries $\partial\Omega^{(i)}$ may have a complex shape.

The finite element mesh for a sub-domain $\Omega^{(i)}$ is based on a fundamental mesh

$$\mathcal{T}(\Omega) = \{E_0, \ldots, E_{M-1}\} \tag{3}$$

of the whole domain Ω.

Based on (3) the triangulation

$$\mathcal{T}(\Omega^{(i)}) = \left\{ E_n^{(i)} = \Omega^{(i)} \cap E_n \,\middle|\, E_n^{(i)} \neq \varnothing \right\} \tag{4}$$

is defined as the intersection of $\Omega^{(i)}$ and the fundamental mesh, see Fig. 1. Note that the elements $E_n^{(i)}$ can be arbitrarily shaped and in general will not be convex. For each triangulation the internal skeleton is named $\Gamma_{\text{int}}^{(i)}$, with

$$\Gamma_{\text{int}}^{(i)} = \left\{ \gamma_{ef} = \partial E_e^{(i)} \cap \partial E_f^{(i)} \,\middle|\, E_e^{(i)}, E_f^{(i)} \in \mathcal{T}(\Omega^{(i)}),\ E_e^{(i)} \neq E_f^{(i)} \text{ and } |\gamma_{ef}| > 0 \right\}. \tag{5}$$

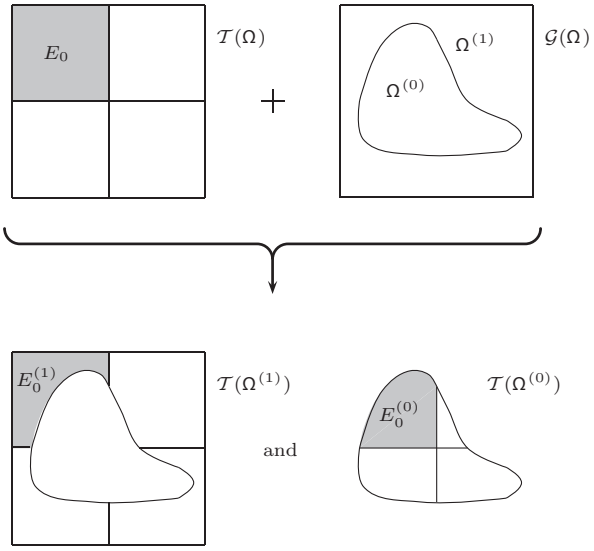

Fig. 1. Construction of the partitions $\mathcal{T}(\Omega^{(i)})$ given the partitions $\mathcal{G}$ and $\mathcal{T}$ of the domain Ω.

Correspondingly, the external skeleton is denoted by

$$\Gamma_{\text{ext}}^{(i)} = \left\{ \gamma_e = \partial E_e^{(i)} \cap \partial\Omega^{(i)} \;\middle|\; E_e^{(i)} \in \mathcal{T}(\Omega^{(i)}) \text{and} |\gamma_e| > 0 \right\}. \tag{6}$$

On the fundamental element E_n, $\varphi_{n,j} \in P_k$ denotes a polynomial, where P_k is the space of polynomial functions of degree k. The shape functions $\varphi_{n,j}^{(i)}$ are given by polynomials $\varphi_{n,j} \in P_k$ with their support restricted to $E_n^{(i)} \in \mathcal{T}(\Omega^{(i)})$. The resulting finite element space is defined by

$$V_k^{(i)} = \left\{ v \in L_2(\Omega^{(i)}) \,\middle|\, v|_{E_n^{(i)}} \in P_k \right\} \tag{7}$$

and is discontinuous on the internal skeleton $\Gamma_{\text{int}}^{(i)}$. The discontinuity of a function $x \in V_k^{(i)}$ evaluated on the interface between two adjacent elements $E_n^{(i)}$ and $E_m^{(i)}$ is denoted by

$$[\![x]\!] = x|_{\partial E_n^{(i)}} \mathbf{n}_{E_n^{(i)}} + x|_{\partial E_m^{(i)}} \mathbf{n}_{E_m^{(i)}}. \tag{8}$$

On the boundary $\partial\Omega^{(i)}$ we define $[\![x]\!]$ to be $[\![x]\!] = x\mathbf{n}_{E_n^{(i)}}$. The average of $x \in V_k^{(i)}$ on the interface is

$$\{x\} = \frac{1}{2}\left(x|_{\partial E_n^{(i)}} + x|_{\partial E_m^{(i)}} \right). \tag{9}$$

On $\partial\Omega^{(i)}$ the average is defined as $\{x\} = x$.

Assembling the local stiffness matrix in a DG approach requires integration over the volume of each element $E_n^{(i)}$ and its surface $\partial E_n^{(i)}$. Mesh elements obtained by the UDG method might exhibit very complicated shapes, thus quadrature rules based on interpolation functions are not directly applicable.

In order to guarantee accurate evaluation of integrals in an efficient way we construct quadrature rules for irregular shaped elements using a local triangulation of $E_n^{(i)}$. To do so, $E_n^{(i)}$ is subdivided into a disjoint set $\{E_{n,k}^{(i)}\}$ of simple geometric objects, i.e. simplices and hypercubes, where each of these can be integrated using efficient Gaussian type quadrature rules. How exactly the local triangulation is constructed, depends on the way the geometry is represented.

3.2. Representation of the domain geometry

The partition $\mathcal{G}(\Omega)$ describes the geometrical information. In [6] two different approaches for a representation of the geometric information are described. The geometry can either be given explicitly, e.g. as CAD primitives, or it can be given implicitly.

In this paper we use an implicit description of the geometry as an iso-surface of a scalar function Φ. This representation is well suited for geometric information obtained as image or voxel data, or for interfaces given by level-set or phase-field methods. The partition $\mathcal{G}$ only contains two sub-domains the void space $\Omega^{(0)}$ and the bulk material $\Omega^{(1)}$.

The scalar function Φ is given as a piecewise linear function on a structured mesh of mesh width $h_{\mathcal{G}}$ and the domain interface $\Gamma^{(0,1)} = \partial\Omega^{(0)} \cap \partial\Omega^{(1)}$ is described by the zero iso-surface. As Φ is piecewise linear the boundary of $\Omega^{(i)}$ must be of polygonal shape.

For the geometry representation using a scalar function, the local triangulation is based on a modified *Marching Cubes* algorithm, which was developed to give a reconstruction of an iso-surface of a scalar function (for details see [10]).

3.3. Discretization of the model problem

The space discretization uses the new UDG approach. The DG discretization of the transport equation follows the formulation in [7]. For the elliptic part $-\nabla \cdot D(\mathbf{u})\nabla c$ the OBB scheme is chosen, which allows higher-order discretization and fulfills the discrete local mass conservation. This scheme uses a penalty term for stabilization. The hyperbolic part $\nabla \cdot \mathbf{u}c$ is discretized using a flux based *Upwind* scheme and does not need additional stabilization. Second order trial and test functions are used. For the OBB scheme we obtain a scheme which is second order accurate in L_2- and H^1-norm.

For time discretization the implicit θ-scheme is used, depending on the choice of θ the scheme is either a first or a second order method.

Note that for the UDG scheme the size of a single element is not bounded from below. The size $h_{\mathcal{T}}$ of most elements will be equal to the mesh width of the fundamental mesh, but the size of some elements can be several orders of magnitude smaller. Explicit time discretization schemes have to fulfill a stability condition, which makes the time step depend on the smallest $h_{\mathcal{T}}$ in the mesh, thus they are not suitable in such a setup.

3.4. θ-Scheme time discretization

Given a linear ordinary differential equation

$$\frac{d}{dt}x = L(t, x), \tag{10}$$

and an initial value $x(0) = x_0$, the solution x on the time interval $[0, T]$ is requested. The interval is subdivided into $0 = t^0 < t^1 < \cdots < t^M = T$ with $\Delta t^n = t^{n+1} - t^n$. The approximation of x^{n+1} by the one-step-θ-scheme is given as

$$x^{n+1} - \Delta t^n\, \theta L(t^{n+1}, x^{n+1}) = x^n + \Delta t^n\, (1-\theta) L(t^n, x^n). \tag{11}$$

The one-step-θ-scheme is parameterized by the coefficient $\theta \in [0, 1]$. For $\theta = 0$ the explicit Euler scheme is obtained, for $\theta = 1$ the scheme is identical to implicit Euler. The scheme with $\theta = 1/2$ is known as *Crank–Nicolson* and is second order accurate.

In order to benefit from the higher order discretization in space we use in the following computation $\theta = 1/2$, i.e. Crank–Nicolson. Although the method is unconditionally stable it must be noted that it is not reasonable to take very large time steps as the approximation error increases. Thus the time step is chosen such that $\mathbf{u}\Delta t < h_{\mathcal{T}}$ is fulfilled on the fundamental mesh. This corresponds to a Courant number of 1 on the fundamental mesh.

3.5. Discontinuous Galerkin discretization of the transport equation

The underlying DG discretization of the transport equation uses the formulation described in [7].

The velocity $\mathbf{u}$ is either given explicitly or obtained from previous computations. On the skeleton $\Gamma^{(0)}$ of $\Omega^{(0)}$ the velocity is defined as the average

$$\mathbf{u}|_\gamma = \{\mathbf{u}\}, \quad \gamma \in \Gamma^{(0)}. \tag{12}$$

The concentration c is given element-wise. The solution $c|_\gamma$ on the skeleton is chosen as the upwind solution c^*. For $\gamma_{ef} \in \Gamma^{(0)}_{\text{int}}$ c^* is given as

$$c|_{\gamma_{ef}} = c^*(x) = \begin{cases} c|_e(x) & \text{if } \mathbf{u}|_{\gamma_{ef}} \cdot \mathbf{n}_e > 0 \\ c|_f(x) & \text{else,} \end{cases} \tag{13}$$

where e and f denote the two elements sharing γ_{ef}. For $\gamma \in \Gamma^{(0)}_D$ the upwind solution is

$$c|_\gamma = c^*(x) = \begin{cases} c(x) & \text{if } \mathbf{u}|_\gamma \cdot \mathbf{n} > 0 \\ c_0(x) & \text{else.} \end{cases} \tag{14}$$

The space discretized problem reads: Find c such that

$$\partial_t m(c, v) + a(c, v) = l(v) \qquad \forall v \in V^{(0)}_k, \tag{15}$$

with the bilinear forms a and m, and the linear form l. Contributions to $a(c, v)$ and to $l(v)$ origin in the elliptic (a_1, l_1) as well as the hyperbolic part (a_2, l_2). The time derivative term is denoted by $m(\cdot, \cdot)$.

The elliptic part is discretized using the OBB scheme. The discretization yields

$$\begin{aligned} a_1(c, v) = &\int_{\Omega^{(0)}} D\nabla c \cdot \nabla v \, dx - \int_{\Gamma^{(0)} \setminus \Gamma^{(0)}_N} [\![c]\!] \cdot \{D\nabla v\} \, ds \\ &+ \int_{\Gamma^{(0)} \setminus \Gamma^{(0)}_N} [\![v]\!] \cdot \{D\nabla c\} \, ds - \int_{\Gamma^{(0)}_D} v D\nabla c \cdot \mathbf{n} \, ds. \end{aligned} \tag{16}$$

The contribution of the elliptic part to the right hand side is

$$l_1(v) = \int_{\Omega^{(0)}} qv \, dx + \int_{\Gamma^{(0)}_D} c_0 D\nabla v \cdot \mathbf{n} \, ds \, . \tag{17}$$

The discretization of the hyperbolic part is obtained straight forward. Applying integration by parts and substituting $c|_\gamma$ and $\mathbf{u}|_\gamma$ according to (13), (14), and (12) yields

$$a_2(c, v) = -\int_{\Omega^{(0)}} \mathbf{u} \, c \, \nabla v \, dx + \int_{\Gamma^{(0)} \setminus \Gamma^{(0)}_N} [\![v]\!] \cdot \{\mathbf{u}\} \, c^* ds. \tag{18}$$

The Neumann boundary condition contributes to the right hand side

$$l_2(v) = -\int_{\Gamma^{(0)}_N} Fv \, ds. \tag{19}$$

4. Results and discussion

The discretization is first applied to two test problems with known analytic solution. Both problems are tested in 2D and 3D and the convergence of the L_2-error is studied. Then we investigate a setup similar to ones used in experiments. Simulations then yield a macroscopic breakthrough curve. In all examples second order shape functions and the Crank–Nicholson time stepping scheme are used.

To investigate grid convergence we look at the experimental order of convergence (EOC). Given two triangulations $\mathcal{T}_1$ and $\mathcal{T}_2$ with distinct mesh widths $h_{\mathcal{T}_1}$ and $h_{\mathcal{T}_2}$ and corresponding solutions with errors e_1 and e_2 the EOC between those meshes is given as

$$\text{EOC} = \frac{\log e_1 - \log e_2}{\log h_{\mathcal{T}_1} - \log h_{\mathcal{T}_2}}. \tag{20}$$

Since the employed method is second order accurate, the expected order of convergence is EOC = 2.

For the computation of the L_2-error a reference solution is needed to compare with. For the first two test cases analytic solutions are available which can be used as the reference solution.

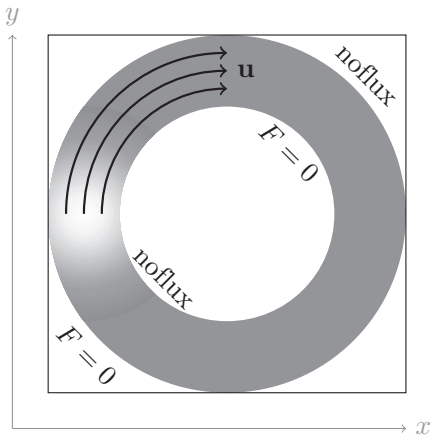

Fig. 2. The "circular channel" setup in 2D. A circular channel with inner diameter 0.6 and outer diameter 1. No-flux boundary conditions are imposed.

4.1. Test problems with analytical solution

The two test setups are a Gaussian peak rotating in a circular channel (Fig. 2), and a Gaussian pulse moving along a tilted channel (Fig. 4). For both setups the domain Ω is the unit square in 2D, respectively the unit cube in 3D.

4.1.1. Circular channel

In 2D the circular channel has an outer diameter of 1 and an inner diameter of 0.6. No-flux boundary conditions are imposed on all boundaries, the velocity field is pointing clockwise along the channel and its magnitude is proportional to the distance from the center, i.e. the angular velocity is constant. At $t = 0$ the concentration forms a Gauss pulse with a width of $\sigma_0 = 0.05$ in the left side of the channel. For 3D the domain is simply extended into the z direction. In this direction the Gaussian pulse is located at $z = 0.5$.

We only consider the pure hyperbolic case without diffusion. At $t = \pi/4$ the pulse is transported exactly to the top of the domain and the error is measured in the L_2-norm. The element size for the different meshes ranges from $h_\mathcal{T} = 1/2$ to $h_\mathcal{T} = 1/1024$ in 2D and to $h_\mathcal{T} = 1/64$ in 3D. The geometry of the channel is described on a grid with $h_\mathcal{G} = h_\mathcal{T}/4$. Note that in this case the geometry is not represented exactly as the scalar function Φ is piecewise linear.

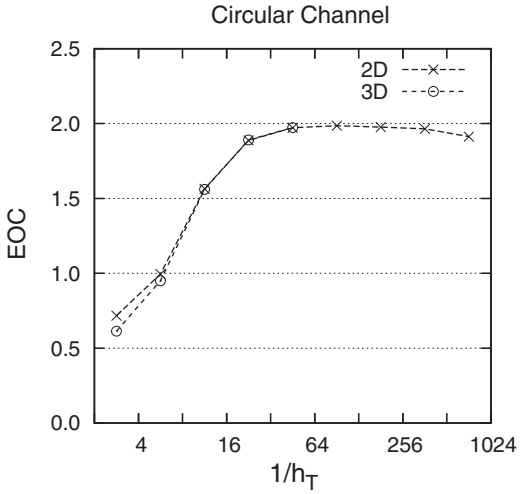

Fig. 3. Experimental order of convergence of the L_2-error for the 2D and 3D pure-convection problem in "circular channel" (Fig. 2). Theoretically expected convergence rates are obtained.

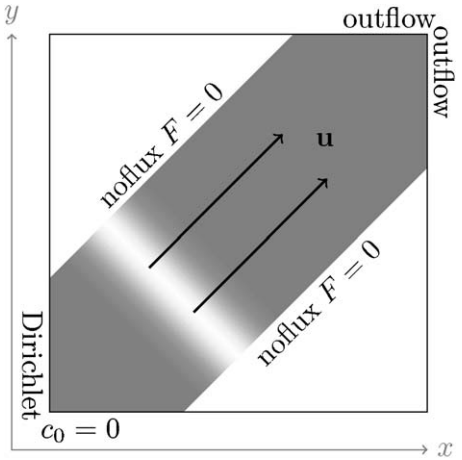

Fig. 4. The "tilted channel" setup in 2D. The lower right and upper left corners of the unit square are cut of. Boundary conditions are no-flux on the cut boundaries, outflow on the top and right boundaries, and Dirichlet ($c_0 = 0$) on the bottom and left boundaries.

The obtained convergence rates are shown in Fig. 3. For both cases, 2D and 3D, second order convergence is obtained for sufficiently small $h_{\mathcal{T}}$.

4.1.2. Tilted channel

In 2D the tilted channel is a unit square, where the lower right and upper left corners are cut of, leaving a channel of width 0.5. Boundary conditions are no-flux on the cut boundaries, outflow on the top and right boundaries, and Dirichlet ($c_0 = 0$) on the bottom and left boundaries. The diffusion coefficient is $D = 10^{-3}$, the velocity vector is $\mathbf{u} = \sqrt{1/2}\,(1, 1)^T$ and the initial concentration is a Gaussian pulse perpendicular to the velocity vector at a distance of 0.25 from the center. The 3D domain is again simply the extension into the third dimension.

The element size for the different meshes ranges from $h_{\mathcal{T}} = 1/2$ to $h_{\mathcal{T}} = 1/1024$ in 2D and $h_{\mathcal{T}} = 1/128$ in 3D. Like in the circular channel setup, the geometry is described on a mesh with $h_{\mathcal{G}} = h_{\mathcal{T}}/4$, here the representation of the domain is exact.

At $t = 0.5$ the pulse has moved a distance of 0.5 and the L_2-error is evaluated. The resulting convergence rates are shown in Fig. 5. Again the predicted convergence rates of EOC = 2 are obtained.

4.2. Example application: solute transport in a porous medium

Breakthrough curves of a tracer are a macroscopic property often measured during experiments. As a more realistic example we compute this property using direct simulation of the pore scale convection–diffusion problem. The tracer flux is measured at the outlet and plotted over the time to obtain the breakthrough curve.

The domain considered here is a channel of size $2 \times 1 \times 1$ partially filled with randomly packed spheres, see Fig. 6. 100 spheres with a radius of 0.095 are randomly packed in the in the central region $0.5 \lesssim x \lesssim 1.5$. Similar setups are also used in experiments, e.g. [21], but usually they contain a lot more spheres.

Boundary conditions are Dirichlet ($c_0 = 0$) on the left boundary, outflow (no boundary condition) on the right boundary and no-flux ($F = 0$) on all other boundaries, including the surface of the spheres. The velocity field is given as the solution of the Stokes equations on the pore scale domain. For the discretization of the Stokes problem we are using the UDG [11] method on a mesh with $h_{\mathbf{u}} = 1/64$, the DG formulation follows the one described in [20]. In the Stokes problem a macroscopic pressure gradient is pointing from left to right. Initial condition for the transport problem is $c = 1$ in the region $[0.125, 0.375] \times [0.25, 0.75]^2$ and $c = 0$ else. The diffusion coefficient is $D = 10^{-5}$.

If the geometry would be obtained from an imaging process, e.g. X-ray tomography, it makes sense to use always a representation of the geometry on the finest mesh. We describe the spheres by a signed distance function on a fine mesh with $h_{\mathcal{G}} = 1/64$ for all values of $h_{\mathcal{T}}$. The obtained geometry is assumed to be the exact geometry.

Simulations are carried out for different mesh sizes, varying from $h_{\mathcal{T}} = 1/8$ to $h_{\mathcal{T}} = 1/64$. In the last case the fundamental mesh $\mathcal{T}$ is the same as the mesh for the geometry. All simulations use the same velocity field. The linear

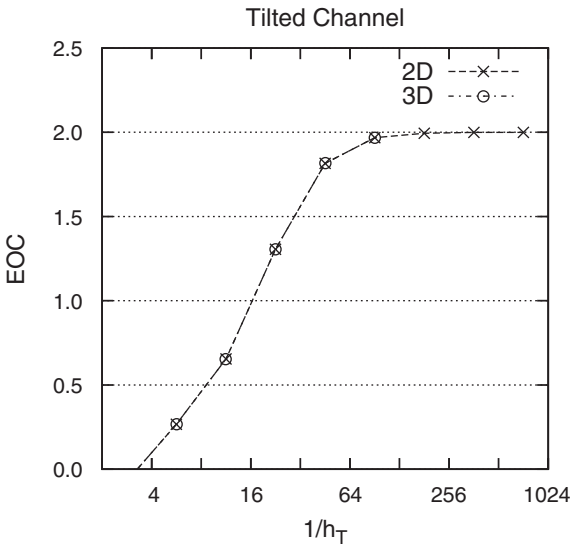

Fig. 5. Experimental order of convergence of the L_2-error for the 2D and 3D transport problem with diffusion $D = 10^{-3}$ in a "tilted channel" (Fig. 4). Theoretically expected convergence rates are obtained.

system was solved using a BiCG-STAB solver with a reduction of 10^{-10} and an ILU preconditioner. The number of degrees of freedom for the different mesh sizes is given in Table 1. For $h_T = 1/64$ the number of iterations for the solver ranges from 9 to 14.

Breakthrough curves of the total concentration flow are computed and plotted in Fig. 7. Numerically the breakthrough values are evaluated as

$$\frac{\int_A \{\mathbf{u}\} \cdot \mathbf{n}\, c^*(t)\, dx}{\int_A \{\mathbf{u}\} \cdot \mathbf{n}\, dx}, \tag{21}$$

where A is a plane perpendicular to the x-axis at $x = 1.75$, and $\mathbf{n}$ its normal vector.

These curves are then used to calculate the L_2-error and the EOC in Table 1, using the result from the mesh with the smallest elements ($h_T = 1/64$) as a the reference solution. Also for this example without analytic solution, the predicted convergence rate of EOC = 2 is obtained. It should be noted that important qualitative features like the tailing can be captured already with a very coarse discretization. The results show further that error in the simulation with $h_T = 1/32$ compared to the highest resolution of $h_T = 1/64$ is not visible and a lot smaller than the expected measurement errors. Already with the very coarse discretization of $h_T = 1/16$ the method gives reliable, good quality

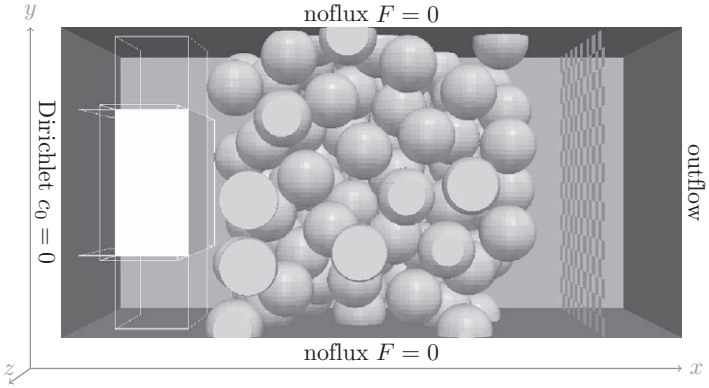

Fig. 6. Setup with an artificial porous medium. The domain has size $2 \times 1 \times 1$. The spheres in the central region approximate the porous medium. Boundary conditions are Dirichlet ($c_0 = 0$) on the left boundary, outflow on the right boundary and no-flux ($F = 0$) on all other boundaries, including the surface of the spheres. Flow is from left to right. The checkered plane to the right indicates where breakthrough curves are obtained.

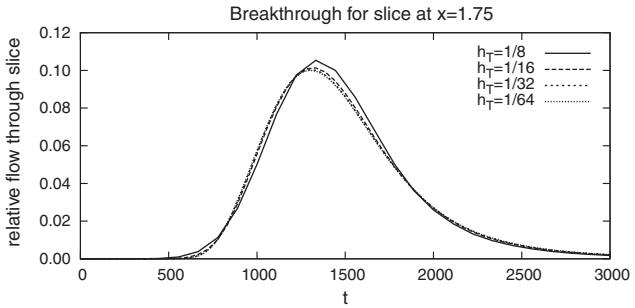

Fig. 7. Breakthrough curves obtained according to (21) for a plane at $x = 1.75$ (checkered plane in Fig. 6). The curves for $h_T = 1/32$ and $h_T = 1/64$ are so much alike that it is very difficult to distinguish them.

Table 1
Number of degrees of freedom, grid Péclet number and experimental order of convergence for the breakthrough curves from Fig. 7. For the L_2-error the breakthrough curve from the finest mesh ($h_T = 1/64$) is used as the reference solution. The last column shows the EOC between the previous and the current row.

$1/h_T$	#dofs	$\mathrm{Pe}_{\mathrm{grid}}$	L_2-error	EOC
8	10240	13.6	0.173	–
16	81920	6.79	0.0500	1.79
32	655360	3.39	0.0127	1.98
64	5242880	1.70	–	–

results. The breakthrough curves show a non-Gaussian shape and a noticeable tailing thus the solute transport is still in the range of anomalous dispersion.

5. Conclusions

In this paper we presented an Unfitted Discontinuous Galerkin (UDG) method for the convection–diffusion equation. It allows the direct simulation of transport processes on the pore scale, using state of the art numerical methods. A second order accurate Discontinuous Galerkin scheme is used for the spatial discretization. As the size h_T of the smallest element in a UDG mesh is not bounded from below explicit time stepping schemes are not suitable and the implicit Crank–Nicholson scheme is employed.

The implementation is based on the DUNE framework [5,4]. For 2D and 3D second order convergence of the L_2-error was observed for two test problems with full regularity, analytically given velocity fields, and known solutions. Detailed simulations on the pore scale as well as measurements of macroscopic quantities like breakthrough curves are possible. As an application example breakthrough curves were computed from full 3D pore scale simulations on an artificial pore structure. Grid convergence for this macroscopic property is observed.

These results show the ability of the UDG method to give reliable numerical results for macroscopic parameters already for a relatively coarse grid. The computation of macroscopic quantities allows comparison with experiments and thus can aid in the verification of macroscopic models.

Computation of parameters for multiphase flow are planned for future work. Using experimentally obtained pore space domains and evolving surfaces will increase the computational demands. Thus the parallelization of the UDG assembler and the coupling with modern domain decomposition methods is the next logical step.

References

[1] R.C. Acharya, S.E.A.T.M. van der Zee, A. Leijnse, Approaches for modeling longitudinal dispersion in pore-networks, Advances in Water Resources 30 (2007) 261–272.

[2] D.N. Arnold, F. Brezzi, B. Cockburn, L.D. Marini, Unified analysis of discontinuous Galerkin Methods for elliptic problems, SIAM Journal on Numerical Analysis 39 (5) (2002) 1749–1779.

[3] J.W. Barrett, C.M. Elliott, Fitted and unfitted finite-element methods for elliptic equations with smooth interfaces, IMA Journal of Numerical Analysis 7 (3) (1987) 283–300.
[4] P. Bastian, M. Blatt, A. Dedner, C. Engwer, R. Klöfkorn, R. Kornhuber, M. Ohlberger, O. Sander, A generic grid interface for parallel and adaptive scientific computing. Part II: Implementation and tests in DUNE, Computing 82 (2–3) (2008) 121–138.
[5] P. Bastian, M. Droske, C. Engwer, R. Klöfkorn, T. Neubauer, M. Ohlberger, M. Rumpf, Towards a unified framework for scientific computing, in: Proceedings of the 15th Conference on Domain Decomposition Methods, Lecture Notes in Computational Science and Engineering, 2004.
[6] P. Bastian, C. Engwer, An unfitted finite element method using discontinuous Galerkin, International Journal for Numerical Methods in Engineering 79 (12) (2009) 1557–1576.
[7] P. Bastian, B. Rivière, Discontinuous Galerkin methods for two-phase flow in porous media, Tech. Rep. 2004–28, IWR (SFB 359), Universität Heidelberg (2004).
[8] L.A. Dillard, M.J. Blunt, Development of a pore network simulation model to study nonaqueous phase liquid dissolution, Water Resources Research 36 (2) (2000) 439–454.
[9] G. Drazer, J. Koplik, Tracer dispersion in two-dimensional rough fractures, Physical Review E 63 (056104) (2001) 1–11.
[10] C. Engwer, An unfitted discontinuous Galerkin scheme for micro-scale simulations and numerical upscaling, Ph.D. thesis, Universität Heidelberg (2009).
[11] C. Engwer, P. Bastian, S.P. Kuttanikkad, An unfitted discontinuous Galerkin finite element method for pore scale simulations, in: 9th International Workshop on State-of-the-Art in Scientific and Parallel Computing, vol. 6126, Lecture Notes in Computer Science, Springer, 2010.
[12] S. Geller, M. Krafczyk, J. Tölke, S. Turek, J. Hron, Benchmark computations based on Lattice-Boltzmann, finite element and finite volume methods for laminar flows, Computers & Fluids 35 (2006) 888–897.
[13] D. Grubert, Effective dispersivities for a two-dimensional periodic fracture network by a continuous time random walk analysis of single-intersection simulations, Water Resources Research 37 (1) (2001) 41–49.
[14] Q. Kang, P.C. Lichtner, D. Zhang, Lattice Boltzmann pore-scale model for multicomponent reactive transport in porous media, Journal of Geophysical Research 111 (B05203) (2006) 1–12.
[15] Q. Kang, P.C. Lichtner, D. Zhang, An improved lattice Boltzmann model for multicomponent reactive transport in porous media at the pore scale, Water Resources Research 43 (W12S14) (2007) 1–12.
[16] C.P. Lowe, D. Frenkel, Do hydrodynamic dispersion coefficients exist? Physical Review Letters 77 (22) (1996) 4552–4555.
[17] C. Manwart, U. Aaltosalmi, A. Koponen, R. Hilfer, J. Timonen, Lattice-Boltzmann and finite-difference simulations for the permeability for three-dimensional porous media, Physical Review E 66 (016702) (2002) 1–11.
[18] J. Nitsche, Über ein Variationsprinzip zur Lösung von Dirichlet-Problemen bei Verwendung von Teilräumen, die keinen Randbedingungen unterworfen sind, Abh. Math. Sem. Univ. Hamburg 36 (1971) 9–15.
[19] H. Okabe, M.J. Blunt, Prediction of permeability for porous media reconstructed using multiple-point statistics, Physical Review E 70 (2004) 066135.
[20] B. Rivière, V. Girault, Discontinuous finite element methods for incompressible flows on subdomains with non-matching interfaces, Computer Methods in Applied Mechanics and Engineering 195 (2006) 3274–3292.
[21] M. Stöhr, Analysis of flow and transport in refractive index matched porous media, Ph.D. thesis, Institute of Environmental Physics, Department of Physics and Astronomy, University of Heidelberg (2003).
[22] P. Tardif d'Hamonville, A. Ern, L. Dormieux, Finite element evaluation of diffusion and dispersion tensors in periodic porous media with advection, Computational Geosciences 11 (1) (2007) 43–58.
[23] A.M. Tartakovsky, P. Meakin, T.D. Scheibe, R.M.E. West, Simulations of reactive transport and precipitation with smoothed particle hydrodynamics, J. Comput. Phys. 222 (2007) 654–672.
[24] H.-J. Vogel, A numerical experiment on pore size, pore connectivity, water retention, permeability, and solute transport using network models, European Journal of Soil Science 51 (2000) 99–105.
[25] H.J. Vogel, K. Roth, Quantitative morphology and network representation of soil pore structure, Advances in Water Resources 24 (3–4) (2001) 233–242.
[26] X. Zhang, M. Lv, Persistence of anomalous dispersion in uniform porous media demonstrated by pore-scale simulations, Water Resources Research 43 (W07437) (2007) 1–11.
[27] Y. Zhu, P.J. Fox, Simulation of pore-scale dispersion in periodic porous media using smoothed particle hydrodynamics, J. Comput. Phys. 182 (2002) 622–645.